Seismic anisotropy from 6C ground motions of ambient seismic noise

Le Tang[1], Heiner Igel[1], Jean-Paul Montagner[2], Frank Vernon[3]

[1]Department of Earth and Environmental Sciences, Ludwig-Maximilians-Universität München, 80333, Munich, Germany
[2]Institut de Physique du Globe de Paris, Université Paris Cité, 75238, Paris, France
[3]Institute of Geophysics and Planetary Physics, University of California San Diego, La Jolla, CA, USA

Key Points:

- We show a new approach enabling the extraction of local phase velocity from 6C cross-correlation functions from ambient noise data.
- Azimuth-dependent 6C cross-correlation functions allow us to study local seismic anisotropy and its depth dependence.
- Local anisotropy at Piñon Flat Observatory is compatible with compression stress, providing constraints on stress-induced anisotropy.

Corresponding author: Le Tang, Le.Tang@lmu.de

Abstract

We propose a new approach capable of measuring local seismic anisotropy from 6C (three-component translation and three-component rotation) amplitude observations of ambient seismic noise data. Our recent theory demonstrates that the amplitude ratio of 6C cross-correlation functions (CCFs) enables retrieving the local phase velocity. This differs from conventional velocity extraction methods based on travel time. Its local sensitivity kernel beneath the 6C seismometer allows us to study anisotropy from azimuth-dependent CCFs, avoiding path effects. Such point measurements have great potential in planetary exploration, ocean bottom observations, or volcanology. We apply this approach to a small seismic array at Piñon Flat Observatory (PFO) in southern California, array-deriving retrieves rotational ground motions from microseismic noise data. The stress and structure-induced anisotropy is well resolved and compatible with other tomography results, providing constraints on the origin of depth-dependent seismic anisotropy.

Plain Language Summary

In contrast to the well-known translational displacement of seismic waves, rotation measures the angle of rotation of a point in a medium as it deforms. Traditionally, the travel time of cross-correlation functions of translational displacement of ambient seismic noise and its corresponding propagation distance is used to calculate the velocity of the subsurface medium. However, our recent theory shows that the amplitude ratio of translational displacement and rotation allows us to reveal the local velocity of the medium beneath the receiver from ambient seismic noise data and to study anisotropy from earthquake events. This paper points out for the first time that the amplitude observations of 6C cross-correlation functions of ambient seismic noise provide a new approach to measure the azimuth-dependent velocity in anisotropic media.

1 Introduction

Rotational motion, as part of the wavefield gradient, can be measured directly by rotational seismometers at high frequencies (Lefevre, 2014; Bernauer et al., 2021; Zembaty et al., 2021) and in broadband ranges (Igel et al., 2007, 2021). Combining three-component translation and three-component rotation, a single 6C seismometer shows great potential in seismological observations, which can investigate the propagation direction of seismic waves (Yuan et al., 2021; Sollberger et al., 2018) and constrain the local Earth's velocity structure (Igel et al., 2007; Wassermann et al., 2016; Keil et al., 2021; Tang & Fang, 2021b; Fang & Tang, 2021; Tang & Fang, 2023; Tang et al., 2023a, 2023b; Tang & Fang, 2023). The ambient seismic noise, as continuous sources on the Earth, has shown its powerful potential in studying Earth's structure based on conventional translation observations (Aki, 1957; Lobkis & Weaver, 2001; Shapiro et al., 2005; Haney et al., 2012). However, it has been an open scientific challenge whether rotational observations of ambient seismic noise can provide additional constraints for the Earth's interior.

To investigate the potential of rotational observations of ambient seismic noise, only a few studies have conducted theoretical derivations and some preliminary observations. Hadziioannou et al. (2012) made the first attempt to extract the phase velocity of surface waves from ambient noise data by combining the translation and rotation observations. However, the overlap of ambient seismic noise destroys the assumption that the phase velocity extracted by the amplitude ratio is based on a single plane wave, resulting in larger uncertainty (Wassermann et al., 2016) in the phase velocity, making it difficult to monitoring small changes in velocities. Paitz et al. (2019) and Nakahara et al. (2021) carried out theoretical experiments of ambient noise interferometry to investigate the connections between Green's functions and cross-correlation functions or spatial auto-correlation (SPAC) coefficients of rotational ground motions, but ignored the potential of the amplitude. Our

recent theory paper focuses on the amplitude of SPAC coefficients of rotational ambient noise data (Tang & Fang, 2023), which indicates the feasibility of measuring the local phase velocity from amplitude ratios of 6C cross-correlation functions. This approach has a local sensitivity that differs from conventional velocity extraction methods based on travel time or phase difference whose sensitivity mainly distributes along the propagation path. The local sensitivity allows us to monitor the velocity variation of the local structure without considering the path effects of the wave propagation (Tang & Fang, 2023).

Studying local seismic anisotropy (Pham et al., 2010; Tang & Fang, 2021a; Noe et al., 2022) from rotational ground motions can provide additional constraints on the tectonic evolution of the Earth (Tang et al., 2023a). The characteristics of rotational ground motions of surface waves in an anisotropic medium are well resolved in the recent study (Tang et al., 2023b) based on the first-order perturbation theory. It indicates that the azimuth-dependent surface wave dispersion curve can be directly obtained by using the amplitude ratio of translation to rotation or strain, which allows us to investigate the mantle flow and plate deformations (Tang et al., 2023a). Combining our recently proposed rotational ambient noise theory (Tang & Fang, 2023) and rotational anisotropy theory (Tang et al., 2023b), we can study local seismic anisotropy from azimuth-dependent 6C cross-correlation functions.

Since permanent high-sensitivity broadband rotation seismometers do not yet exist, the array-derived rotation (ADR) method is well suited (Spudich et al., 1995; Spudich & Fletcher, 2008; Donner et al., 2017; Tang et al., 2023a) to retrieve the rotational waveform. However, the available period range is generally limited by the aperture of a seismic array, the uncertainty of instruments, and noise level. We select a small seismic array at the Piñon Flat Observatory in southern California to retrieve rotational ground motions and study local seismic anisotropy based on our new method for the first time. Ultimately, such 6C ambient noise data processing would be possible, if sufficiently sensitive sensors for all motion components would exist. This remains a technical challenge (Brotzer et al., 2023).

2 Methods

2.1 Velocity measurement from 6C CCFs

In isotropic media, the phase velocity of surface waves can be extracted from the amplitude ratio of 6C CCFs (Tang & Fang, 2023).

$$\left|\frac{C\dot{C}F_{(V_{z1},V_{z2})}}{CCF_{(V_{z1},\Omega_{t2})}}\right| = c_R \tag{1}$$

$$\left|\frac{C\dot{C}F_{(V_{r1},V_{z2})}}{CCF_{(V_{r1},\Omega_{t2})}}\right| = c_R \tag{2}$$

$$\left|\frac{C\dot{C}F_{(V_{t1},V_{t2})}}{2CCF_{(V_{t1},\Omega_{z2})}}\right| = c_L \tag{3}$$

where V_{z1}, V_{r1} and V_{t1} represent the three-component translational velocity of station-1 (See Figure 1a). V_{z2}, V_{t2}, Ω_{t2} and Ω_{z2} represent the two-component translational velocity and two-component rotational rate of station-2, respectively. CCF represents cross-correlation functions of a pair of stations and the $C\dot{C}F$ is the time derivative. c_R and c_L represent the phase velocity of the Rayleigh wave and Love wave, respectively. Equations (1-3) provide a new approach to measure the phase velocity from 6C CCFs of ambient seismic noise data, whose sensitivity kernel (gray zone in Figure 1a) is located beneath the 6C station (Tang & Fang, 2023; Fichtner & Igel, 2009; Tang et al., 2023a).

2.2 Azimuthal anisotropy from 6C observations

Our recent theory (Tang et al., 2023b) demonstrates that the amplitude ratio of acceleration to rotation rate or strain rate is equal to the theoretical azimuth-dependent phase velocity derived by Smith and Dahlen (1973). In this paper, we only consider the fundamental mode of Rayleigh waves. The dispersion equation of the Rayleigh wave from amplitude observations can be expressed as (Tang et al., 2023b):

$$|\frac{\dot{V}_z(\omega,\psi)}{\Omega_t(\omega,\psi)}| = c_0(\omega) + R_2(\omega)cos(2\psi) + R_3(\omega)sin(2\psi) + R_4(\omega)cos(4\psi) + R_5(\omega)sin(4\psi) \quad (4)$$

where $c_0(\omega) = c_{R0}(\omega) + R_1(\omega)$. $c_{R0}(\omega)$ is the phase velocity of the Rayleigh wave for the isotropic medium considered as a reference model. $\dot{V}_z(\omega,\psi)$ is the first-order time derivative of vertical translational velocity and $\Omega_t(\omega,\psi)$ is the transverse rotational velocity. ψ is the backazimuth of the wavenumber vector measured clockwise from the north direction. $R_i(\omega)$ $(i = 1, 2, 3, 4, 5)$ are respectively depth integration functions that involve some elastic parameters and eigenfunctions, where we used a simple integration expression derived by Montagner and Nataf (1986), whose explicit expressions can be found in Equations (2), (4), and (5) of Montagner and Nataf (1986). Equation (4) provides a new approach for estimating phase velocities in anisotropic media which only depends on amplitude information. Its local sensitivity kernel allows us to monitor the local velocity with high lateral resolution that can be several times smaller than one wavelength (Fichtner & Igel, 2009; Tang & Fang, 2023; Tang et al., 2023b, 2023a). We replace the vertical velocity and transverse rotation velocity in Equation (4) with the corresponding CCFs in Equation (1), which allows us to study azimuthal anisotropy from ambient seismic noise data.

3 Data

The ambient noise data comes from the CI, AE, AZ, PY, BC, and US station networks, SCEDC (Southern California Seismic Network), and IRIS data center. We select 22 three-component stations distributed as evenly as possible around the 6C station (see Figure 1b) and use one-year ambient noise data from February 2015 to February 2016 to calculate cross-correlation functions and investigate the local azimuthal anisotropy. Figure 1b shows the geometry of seismic stations and the red triangle represents the 6C station where black triangles are the distributions of 3C stations. The distance between PFO.6C station and 3C stations can be found in Figure S1, which is from 212km to 512km. Considering that broadband rotational seismometers have not been permanently deployed widely, we select three-component broadband seismometers at Piñon Flat Observatory in southern California as the reference 6C array (see Figure 1c) to retrieve rotational ground motions using the ADR approach (Spudich et al., 1995; Spudich & Fletcher, 2008; Tang et al., 2023a) from ambient seismic noise data. The period range of wavefield gradients from PFO.6C array (the aperture is about 500m) in Figure 1c is about 3-50s (Donner et al., 2017) allowing the retrieval of rotational motions from two dominant microseismic noise data (5-10s: Secondary microseismic noise. 10-20s: Primary microseismic noise).

The ambient noise data processing workflow of the 3C station and the 6C station are different. The 3C station can completely follow the processing steps summarized by Bensen et al. (2007). Here, we perform one-bit normalization for 3C stations. In contrast, the 6C station requires different amplitude normalization, whose processing workflow (see Figure 2) generally includes: (1) Remove instrument response, remove trend, remove mean, cut the data to a certain length (e.g. 1 hour or 1 day) and we filter the two dominant microseismic noise data of the PFO.6C station into two frequency ranges: 7s-12s and 12s-20s, because the period range of 5-6s contains strong scattered waves in CCFs of station pairs perpendicular to the coastline direction. (2) Amplitude normalization in the time domain: we perform absolute mean normalization to all components by running a time window (width: 5-10s).

It must be emphasized that all components should be normalized by the same absolute mean (see Figure 2), where we calculate the absolute mean using rotational components (e.g. Rayleigh wave: Ω_t and Love wave: Ω_z). (3) Calculate the CCFs and stacking. (4) Extract the phase velocity based on Equations (1-3). Among them, step (2) is to preserve the amplitude ratio information during data processing, because the phase velocity only comes from the contribution of the 6C station (Tang & Fang, 2023).

4 Results

4.1 Retrieval of 6C CCFs

Due to the high-quality waveform requirement of our approach, it is better to choose Equation (1) instead of Equation (2) to calculate the CCFs of Rayleigh waves, because V_z and Ω_t are only associated with Rayleigh waves in isotropic media and the coupling effect is very small and can be neglected for the fundamental mode in weakly anisotropic media (Tang et al., 2023b). In contrast, V_r also records ambient Love waves that will contaminate the waveform of Rayleigh waves and affect the signal-to-noise ratio (Tang et al., 2023b).

Figure 3 shows the retrieved CCFs of Rayleigh waves of 7-12s using five pairs of stations (CI.DSC, CI.PDM, CI.OLP, CI.SDD, CI.SBB2 and PFO.6C station) at different azimuths based on Equation (1), in which red lines in Figure 1b represent their great circle paths. The 22 pairs of CCFs (see Figure 1b) in azimuth domains for two different frequency ranges are shown in Figure 4 (7-12s) and Figure 5 (12-20s). The very high correlation in the period range of 7-12s between translation-based CCFs and rotation-based CCFs (see Figure 3 and Figure 4) indicates the applicability of retrieved rotational waveform from the ADR approach, making it possible to extract the velocity from the amplitude ratio. This point is further elaborated in the Discussion section.

However, in some azimuths, such as around 130-150 degrees and 340 degrees (see Figure 4), the noise interference of the cross-correlation function is strong, which is related to the distribution of secondary microseismic noise at 7-10s mainly coming from 180-270 degrees backazimuths (Schulte-Pelkum et al., 2004; Stehly et al., 2006). The distribution of primary microseismic noise at 12-20s is relatively complex, accompanied by strong seasonal variations (Stehly et al., 2006), resulting in low signal-to-noise ratios of CCFs and low correlation between translation-based CCFs and rotation-based CCFs (see Figure 5).

The asymmetric CCFs of 7-12s in Figure 3 and Figure 4 indicate the inhomogeneity of the secondary microseismic noise, mainly originating in the direction of the Pacific Ocean (Stehly et al., 2006). From a theoretical point of view, the choice of positive or negative part of the cross-correlation function is necessary for estimating azimuth-dependent phase velocity, since the noise sources corresponding to these two parts come from the symmetry direction and the extracted phase velocity by the two parts have symmetrical azimuths. For example, one is 0 degrees and the other is 180 degrees.

As illustrated in Figure 3 and Figure 4, the ambient noise of 7-12s mainly comes from one direction of the station pair. To have better azimuth coverage and to apply to most cases where the cross-correlation function of ambient seismic noise is asymmetric, we give a reasonable assumption here that Earth's anisotropic medium has a horizontal axis of symmetry, corresponding to a horizontal transversely isotropic (HTI) medium. Under this assumption, the Rayleigh wave phase velocities estimated by the positive and negative parts of the cross-correlation function are equal. Therefore, we can select any waveform of the positive and negative parts of the cross-correlation function to extract the velocity and regard the direction from the 3C station to the 6C station as the azimuth of the phase velocity.

4.2 Velocity estimation and azimuthal anisotropy

As illustrated in Equations (1-3) and (4), amplitude ratios of CCFs enable extracting local phase velocity and allow us to study the local seismic anisotropy utilizing CCFs at different azimuths. We use the least-square method introduced by Tang et al. (2023b) to estimate the phase velocity of the Rayleigh wave using the waveform in Figure 4 and Figure 5 based on Equation (1). As shown in Figure 6, the calculated average phase velocity from 22 pairs of CCFs marked by a black solid line is compatible with the isotropic PREM (Preliminary Reference Earth Model) (Dziewonski & Anderson, 1981), but slightly faster because the PFO array is located over metamorphic rocks and granite, at an elevation of about 1.2km (see Figure 1b). However, compared with the uncertainty (1σ) of 0.2km/s-0.3km/s at the period range of 7-12s, the period range of 13-20s shows a large uncertainty around 0.3km/s-0.6km/s, which not only indicates the velocity anisotropy but is also mainly contaminated by waveform errors related to complex ambient noise distributions (see the discussion section), leading to the low waveform correlation and low signal-to-noise ratio (see Figure 5). Therefore, we only focus on the period range of 7-12s for our anisotropy study.

To investigate the azimuth-dependent variation in phase velocity, we average the velocity estimates in 60-degree azimuth bins. Figure 7 shows the measured phase velocity variation using one-year (2015.02-2016.02) ambient noise data at 6 periods where the isotropic term $c_0(\omega)$ in Equation (4) is subtracted. The red and blue curves in Figure 7 are the best-fit curves for 2ψ and $2\psi + 4\psi$ terms of Equation (4), respectively. It can be seen that the estimated phase velocity matches with the 2ψ and $2\psi + 4\psi$ anisotropy term and the difference between the two curves is very small. From a theoretical point of view, the 4ψ anisotropy term for Rayleigh waves is quite small as demonstrated by Montagner and Nataf (1986) and can be neglected in many anisotropy observations. However, in our study, we also analyze the 4ψ term, as the extensive distribution of faults, complex stress compression, and plate deformation in southern California make the structure extremely complex (Tape et al., 2009; Alvizuri & Tanimoto, 2011; Tang et al., 2023a).

Even though the secondary microseismic noise (5-10s) in southern California does not show seasonal variations (Stehly et al., 2006) in the phase, it is still necessary to investigate the effect of seasonal noise distributions on velocity measurements, as the amplitude change is visible (Stehly et al., 2006) with a different signal-to-noise ratio probably leading to considerable velocity errors. As indicated in Figure 8a, the peak-to-peak anisotropy fluctuates between around 4%-7% over one year, whose difference in anisotropy between spring-summer and autumn-winter (see Figure S2 for seasonal velocity variations in the backazimuth domain) is probably due to slight changes in the distribution of noise sources. However, the estimated fast axis direction of 2ψ+4ψ term in Figure 8b is relatively stable within a year. The fast axis direction of 7s mainly points to the north-south direction (-10-0 degrees), the 10s fluctuate between 0-10 degrees, and the 12s fluctuate in the backazimuth of 10-20 degrees. Considering the seasonal effect, we average the result of one year in Figure 8 to obtain a reliable anisotropy and fast axis (see Figure 9). As indicated in Figure 9a, the anisotropy weakens with increasing period, mainly distributed between 4%-7% and the fast axis (see Figure 9b) shows a clear transition from north-south to northeast-southwest direction.

5 Discussion

5.1 Stability of velocity measurement based on 6C CCFs

It is very dangerous to use the waveforms of single earthquake events to estimate the velocity from 6C amplitude ratios, since a small disturbance, probably from the uncertainty of instruments or random noise, on the waveform will have a considerable impact on the amplitude ratio (Kurrle et al., 2010). Therefore, waveform stacking of a large number of

events is required to obtain a reliable result (Tang et al., 2023b, 2023a). The continuous ambient noise data provides the feasibility of obtaining a reliable solution after ambient seismic noise stacking for several months. To investigate the robustness of the proposed approach based on amplitude observations, we calculate three variables (signal-to-noise ratio (SNR), correlation coefficients between translation-based CCFs and rotation-based CCFs, and relative velocity variation) for one pair of stations (CI.PDM and PFO.6C in Figure 1b with 69.4 degrees backazimth) shown in Figure 10 to assess how they change during one-year ambient noise data.

With the continuous stacking of ambient noise data, the SNR of CCFs increases to about 20-30 in one year (see Figure 10a) while the SNR of 7s, 10s and 12s is higher than that of 15s because of the higher energy of the secondary microseism noise compared with the primary microseism noise. As shown in Figure 10b, the corresponding cross-correlation coefficient increases slightly with the addition of data. However, it can be seen that even if the correlation between the rotation-based CCFs and the translation-based CCFs has reached more than 99%, the extracted phase velocity of the first month by the amplitude ratio still fluctuates in a large range as shown in Figure 10c. Therefore, the cross-correlation coefficient cannot be completely relied on as the only criterion for judging and selecting high-quality waveform, which is only one important indicator for evaluating waveform. The obvious improvement of the SNR and the gradual convergence of the corresponding phase velocity after more data stacking (see Figures 10a and 10c) imply the necessity of higher SNR for amplitude-based velocity measurements. After about three months of data stacking, the relative change in velocity gradually decreases (see Figure 10c), and the phase velocity converges to a stable value, especially for 7-12s, indicating the feasibility of obtaining a stable and reliable phase velocity through the amplitude ratio of CCFs after ambient noise stacking of several months.

It should be noted that the stable solution of the analyzed station pair only indicates that a stable solution can be obtained on the premise of obtaining CCFs with a high SNR, and it is also applicable to long periods (such as 15s in Figure 10). Due to the uneven distribution of ambient noise and seasonal changes, especially the primary microseismic noise in southern California (Stehly et al., 2006), the observation of velocity at 13-20s is not stable at all azimuths (see Figure 6), which is not conducive to the study of anisotropy.

5.2 Effect of noise distribution and coupled waves

The effect of ambient noise distribution on the velocity extraction using the amplitude ratio of CCFs can be divided into two cases. In the first case, noise sources are mainly distributed in the stationary zone on one side of the pair of stations (Campillo et al., 2011). Therefore, the velocity at the symmetric azimuth cannot be obtained which will affect the azimuthal coverage of the anisotropy study. However, we can assume that the symmetry axis of the anisotropic medium is horizontal (velocities at the horizontal symmetry direction are equal) and there is no need to distinguish which direction the noise comes from, just use the azimuth of the station pair. In another case, the noise source is not distributed in the stationary zone (Campillo et al., 2011), which implies that the calculated CCFs are biased in terms of travel time between the two stations. In contrast, the amplitude can be corrected to calculate the local phase velocity, since the amplitude of $CCF_{(V_z,V_z)}$ is not related to the azimuth of noise distribution and $CCF_{(V_z,\Omega_t)}$ in Equation (1) can be replaced by $\sqrt{CCF^2_{(V_z,\Omega_t))} + CCF^2_{(V_z,\Omega_r))}}$ after rotating the two components $CCF_{(V_z,\Omega_t)}$ and $CCF_{(V_z,\Omega_r)}$ into the direction of the maximum amplitude which is similar to the ORA (optimal rotation algorithm) (Roux, 2009). Where the horizontal rotational components Ω_t and Ω_r are dominated by Rayleigh waves (Tang et al., 2023b).

Figure 11 shows the synthetic verification of correcting the source azimuth deviation. As indicated in Figure 11a, the noise source is evenly distributed in azimuth and is approximately 1000km away from two stations (black triangle), with a distance of 100km

between the two stations. Due to the deviation of the noise source, there is a significant difference in their travel time of CCFs (see Figure 11b), making it impossible to extract the velocity between the two stations based on travel time. Similarly, the estimated velocity using Equation (1) is not reliable (black line in Figure 11c). In contrast, azimuth correction using horizontal rotation components $\sqrt{CCF^2_{(V_z,\Omega_t))} + CCF^2_{(V_z,\Omega_r))}}$ allows us to obtain the accurate velocity (blue line in Figure 11c).

However, considering the coupling effect of Rayleigh waves and Love waves in anisotropic media, coupled waves with small amplitudes will be generated on other components of CCFs (Saade et al., 2015). As illustrated in Figure 12, the small amplitude on the $CCF_{(V_z,\Omega_z)}$ probably indicates the coupled wave if the influence of 3D heterogeneous scattering is excluded, since V_z and Ω_z only correspond to Rayleigh waves and Love waves in isotropic media, respectively. Consequently, the small amplitude on $CCF_{(V_z,\Omega_r)}$ (see Figure 12) is the result of a combination of noise source deviation and coupling effects, which indicates that one should be careful to do the noise source correction especially when the azimuth deviation is quite small. Because it is difficult to quantitatively separate the magnitude of the two small amplitudes, further study is needed in the future. As indicated in Figure S3, in most azimuths (0-100 degrees, 180-260 degrees), the angle deviation ($tan\psi = CCF_{(V_z,\Omega_r)}/CCF_{(V_z,\Omega_t)}$) of the noise source is about 10 degrees, which is quite small. Therefore, the estimated phase velocities in Figure 6 and Figure 7 are obtained without azimuth correction. However, the velocity extracted at these azimuths of 130-180 degrees and 270-360 degrees has been corrected because it shows a larger angle deviation (see Figure S3), but its low signal-to-noise and scattered waves lead to larger uncertainty (see Figure 7). Although the azimuth of the noise source at 7-12s can be corrected using the method, the strong seasonal noise variation makes it difficult to obtain a stable solution in the long period range. Therefore, further study is needed for the localization and correction of ambient noise sources, such that the 6C-based cross-correlation technology can be extended to longer period ranges in the future.

5.3 Stress and structure-induced anisotropy from 6C measurements

The lateral resolution of the conventional methods of anisotropy study in southern California is limited by the aperture of stations, wavelength, and strong heterogeneity. In contrast, the unique local sensitivity kernel of our approach allows us to image the local structure and to study local anisotropy (Tang et al., 2023b, 2023a). Here, we estimate the corresponding depth range based on Rayleigh's sensitivity kernel of PREM model at 7s, 10s, 12s and 15s (see Figure S4), indicating that the anisotropy at periods of 7-12s in Figure 7 are most sensitive to the upper 5-20km of the crust. We compare it with other anisotropy results estimated from different methods that have a lateral local sensitivity kernel. The anisotropy strengths measured near the San Andreas Fault indicate that borehole measurements show around 10% anisotropy in the near surface (Aster & Shearer, 1991; Boness & Zoback, 2004), and shear-wave splitting results indicate that the crustal anisotropy is between 8% and 15% (Boness & Zoback, 2006), demonstrating the considerable 4%-7% anisotropy shown in Figure 9. The derived direction of the fast axis (blue line in Figure 13) at 7s sensitive to the upper 5-15km of the crust (see Figure S4) is consistent with the maximum horizontal compression stress (orange lines in Figure 13) (Heidbach et al., 2010) and in agreement with the results of shear-wave splitting in the upper 20km of the crust (yellow line in Figure 13) (Yang et al., 2011) at the PFO station. Its anisotropy is generally interpreted by preferentially aligned cracks or SPO (shape-preferred orientation) that are associated with the stress field (Aster & Shearer, 1991; Boness & Zoback, 2004, 2006; Yang et al., 2011; Wu et al., 2022).

In the depth direction, the fast axis shifts from the north-south direction of the upper crust (blue line in Figure 13) to the northeast-southwest direction of the middle crust (red line in Figure 13), which is consistent with the results obtained by the P-wave tomography method (purple line-a and line-b in Figure 13) (Wu et al., 2022). It provides evidence of layered anisotropy in the upper crust from 5km to 20km, which is probably due to the onset of the transition from stress-induced anisotropy to structure-induced anisotropy.

Because the fast axis in the lower crust by the beamforming tomography result of Rayleigh waves mainly points towards the northeast-southwest direction (Tanimoto & Prindle, 2007), approximately between 40 and 60 degrees (black lines in Figure 13). This anisotropy is generally caused by the crystallographic preferred orientation (CPO) of anisotropic minerals formed during rock formation and subsequent deformation (e.g. (Alvizuri & Tanimoto, 2011; Tanimoto & Prindle, 2007; Wu et al., 2022) for southern California).

6 Conclusion

We propose a new method based on 6C ambient noise data for investigating the local seismic anisotropy. The local seismic anisotropy at Piñon Flat Observatory in southern California in the period range of secondary microseismic noise is resolved, showing stress and structure-induced seismic anisotropy at different depths, providing new insight into the origin of depth-dependent anisotropy. Sufficient ambient seismic noise data and the effective ADR technique enable wide and quick applicability in various seismological studies. We expect the rapid development of high-quality broadband 6C rotational seismometers, which are capable of retrieving rotational waveform based on a single 6C station. Our approach would be particularly useful whenever large seismic arrays are not affordable or difficult to implement (e.g. planetary exploration, ocean bottom observations, volcanology, or urban seismology).

7 Acknowledgments

We thank Michel Campillo (ISTerre, Grenoble) and Eleonore Stutzmann (IPGP, Paris) for constructive discussions. This work is funded by the European Union's Horizon 2020 research and innovation program under the Marie Skłodowska-Curie grant agreement No 955515 (ITN SPIN). HI is grateful for a scholarship by the Cecil and Ida Green Foundation funding his visits to the Institute of Geophysics and Planetary Physics in La Jolla, California in 2022 and 2023.

Open Research

The ambient noise data is publicly available and accessed from CI network (California Institute of Technology and United States Geological Survey Pasadena, 1926) retrieved from $https://doi.org/10.7914/sn/ci$, AE network (Arizona Geological Survey, 2007) retrieved from $https://doi.org/10.7914/sn/ae$, AZ network (Frank Vernon, 1982) retrieved from $https://doi.org/10.7914/sn/az$, PY network (Frank Vernon, 2014) retrieved from $https://doi.org/10.7914/sn/py$, BC network (Centro de Investigación Científica y de Educación Superior de Ensenada (CICESE), Ensenada, 1980) retrieved from $https://doi.org/10.7914-/sn/bc$, and US station network (Albuquerque Seismological Laboratory (ASL)/USGS, 1990) retrieved from $https://doi.org/10.7914/sn/us$. The shear-wave splitting direction is available from Yang et al. (2011) retrieved from $https://doi.org/10.1029/2010JB007655$. Maximum compression stress data is available from Heidbach et al. (2010) retrieved from $https://doi.org/10.1016/j.tecto.2009.07.023$. Fast-axis directions using the surface wave beamforming method are available from Tanimoto and Prindle (2007) retrieved from $https://doi.org/10.1186/BF03352706$. Fast-axis directions of P wave tomography are available from Wu et al. (2022) retrieved from $https://doi.org/10.1029/2022GL100233$. The plate motion directions are available from Tang et al. (2023a) retrieved from $https://doi.org-/10.1029/2023GL105970$.

References

Aki, K. (1957). Space and time spectra of stationary stochastic waves, with special reference to microtremors. *Bulletin of the Earthquake Research Institute*, *35*, 415–456.

Albuquerque Seismological Laboratory (ASL)/USGS. (1990). *United states national seismic network.* International Federation of Digital Seismograph Networks [Dataset]. Retrieved from `https://www.fdsn.org/networks/detail/US/` doi: 10.7914/SN/US.

Alvizuri, C., & Tanimoto, T. (2011). Azimuthal anisotropy from array analysis of rayleigh waves in southern california. *Geophysical Journal International*, *186*(3), 1135–1151.

Arizona Geological Survey. (2007). *Arizona broadband seismic network.* International Federation of Digital Seismograph Networks [Dataset]. Retrieved from `https://www.fdsn.org/networks/detail/AE/` doi: 10.7914/SN/AE.

Aster, R. C., & Shearer, P. M. (1991). High-frequency borehole seismograms recorded in the san jacinto fault zone, southern california. part 1. polarizations. *Bulletin of the Seismological Society of America*, *81*(4), 1057–1080.

Bensen, G., Ritzwoller, M., Barmin, M., Levshin, A. L., Lin, F., Moschetti, M., ... Yang, Y. (2007). Processing seismic ambient noise data to obtain reliable broad-band surface wave dispersion measurements. *Geophysical journal international*, *169*(3), 1239–1260.

Bernauer, F., Behnen, K., Wassermann, J., Egdorf, S., Igel, H., Donner, S., ... others (2021). Rotation, strain, and translation sensors performance tests with active seismic sources. *Sensors*, *21*(1), 264.

Boness, N. L., & Zoback, M. D. (2004). Stress-induced seismic velocity anisotropy and physical properties in the safod pilot hole in parkfield, ca. *Geophysical Research Letters*, *31*(15).

Boness, N. L., & Zoback, M. D. (2006). Mapping stress and structurally controlled crustal shear velocity anisotropy in california. *Geology*, *34*(10), 825–828.

Brotzer, A., Igel, H., Stutzmann, E., Montagner, J., Bernauer, F., Wassermann, J., ... Schreiber, K. U. (2023, 12). Characterizing the Background Noise Level of Rotational Ground Motions on Earth. *Seismological Research Letters*. Retrieved from `https://doi.org/10.1785/0220230202` doi: 10.1785/0220230202

California Institute of Technology and United States Geological Survey Pasadena. (1926). *Southern california seismic network.* International Federation of Digital Seismograph Networks [Dataset]. Retrieved from `https://www.fdsn.org/networks/detail/CI/` doi: 10.7914/SN/CI.

Campillo, M., Roux, P., & Shapiro, N. M. (2011). Seismic, ambient noise correlation. In H. K. Gupta (Ed.), *Encyclopedia of solid earth geophysics* (pp. 1230–1236). Dordrecht: Springer Netherlands. Retrieved from `https://doi.org/10.1007/978-90-481-8702-7_218.` doi: 10.1007/978-90-481-8702-7_218.

Centro de Investigación Científica y de Educación Superior de Ensenada (CICESE), Ensenada. (1980). *Red sísmica del noroeste de méxico.* International Federation of Digital Seismograph Networks [Dataset]. Retrieved from `https://www.fdsn.org/networks/detail/BC/` doi: 10.7914/SN/BC.

Donner, S., Lin, C.-J., Hadziioannou, C., Gebauer, A., Vernon, F., Agnew, D. C., ... Wassermann, J. (2017). Comparing direct observation of strain, rotation, and displacement with array estimates at piñon flat observatory, california. *Seismological Research Letters*, *88*(4), 1107–1116.

Dziewonski, A. M., & Anderson, D. L. (1981). Preliminary reference earth model. *Physics of the earth and planetary interiors*, *25*(4), 297–356.

Fang, X., & Tang, L. (2021). A single station approach for subsurface anomaly detection. In *Seg/aapg/sepm first international meeting for applied geoscience & energy.*

Fichtner, A., & Igel, H. (2009). Sensitivity densities for rotational ground-motion measurements. *Bulletin of the Seismological Society of America*, *99*(2B), 1302–1314.

Frank Vernon. (1982). *Anza regional network.* International Federation of Digital Seismograph Networks [Dataset]. Retrieved from `https://www.fdsn.org/networks/detail/AZ/` doi: 10.7914/SN/AZ.

Frank Vernon. (2014). *Piñon flats observatory array.* International Federation of Digital Seismograph Networks [Dataset]. Retrieved from `https://www.fdsn.org/networks/detail/PY/` doi: 10.7914/SN/PY.

Hadziioannou, C., Gaebler, P., Schreiber, U., Wassermann, J., & Igel, H. (2012). Examining ambient noise using colocated measurements of rotational and translational motion. *Journal of seismology*, *16*, 787–796.

Haney, M. M., Mikesell, T. D., van Wijk, K., & Nakahara, H. (2012). Extension of the spatial autocorrelation (spac) method to mixed-component correlations of surface waves. *Geophysical Journal International*, *191*(1), 189–206.

Heidbach, O., Tingay, M., Barth, A., Reinecker, J., Kurfeß, D., & Müller, B. (2010). Global crustal stress pattern based on the world stress map database release 2008. *Tectonophysics*, *482*(1-4), 3–15. Retrieved from `[Dataset].https://doi.org/10.1016/j.tecto.2009.07.023.`

Igel, H., Cochard, A., Wassermann, J., Flaws, A., Schreiber, U., Velikoseltsev, A., & Pham Dinh, N. (2007). Broad-band observations of earthquake-induced rotational ground motions. *Geophysical Journal International*, *168*(1), 182–196.

Igel, H., Schreiber, K. U., Gebauer, A., Bernauer, F., Egdorf, S., Simonelli, A., ... others (2021). Romy: A multi-component ring laser for geodesy and geophysics. *Geophysical Journal International*.

Keil, S., Wassermann, J., & Igel, H. (2021). Single-station seismic microzonation using 6c measurements. *Journal of Seismology*, *25*(1), 103–114.

Kurrle, D., Igel, H., Ferreira, A. M., Wassermann, J., & Schreiber, U. (2010). Can we estimate local love wave dispersion properties from collocated amplitude measurements of translations and rotations? *Geophysical research letters*, *37*(4).

Lefevre, H. C. (2014). *The fiber-optic gyroscope*. Artech house.

Lobkis, O. I., & Weaver, R. L. (2001). On the emergence of the green's function in the correlations of a diffuse field. *The Journal of the Acoustical Society of America*, *110*(6), 3011–3017.

Montagner, J.-P., & Nataf, H.-C. (1986). A simple method for inverting the azimuthal anisotropy of surface waves. *Journal of Geophysical Research: Solid Earth*, *91*(B1), 511–520.

Nakahara, H., Emoto, K., & Nishimura, T. (2021). Extending the formulation of the spatial autocorrelation (spac) method to strain, rotation and tilt. *Geophysical Journal International*, *227*(1), 287–302.

Noe, S., Yuan, S., Montagner, J., & Igel, H. (2022). Anisotropic elastic parameter estimation from multicomponent ground-motion observations: a theoretical study. *Geophysical Journal International*, *229*(2), 1462–1473.

Paitz, P., Sager, K., & Fichtner, A. (2019). Rotation and strain ambient noise interferometry. *Geophysical Journal International*, *216*(3), 1938–1952.

Pham, N. D., Igel, H., de la Puente, J., Käser, M., & Schoenberg, M. A. (2010). Rotational motions in homogeneous anisotropic elastic media. *Geophysics*, *75*(5), D47–D56.

Roux, P. (2009). Passive seismic imaging with directive ambient noise: application to surface waves and the san andreas fault in parkfield, ca. *Geophysical Journal International*, *179*(1), 367–373.

Saade, M., Montagner, J., Roux, P., Cupillard, P., Durand, S., & Brenguier, F. (2015). Influence of seismic anisotropy on the cross correlation tensor: numerical investigations. *Geophysical Journal International*, *201*(2), 595–604.

Schulte-Pelkum, V., Earle, P. S., & Vernon, F. L. (2004). Strong directivity of ocean-generated seismic noise. *Geochemistry, Geophysics, Geosystems*, *5*(3).

Shapiro, N. M., Campillo, M., Stehly, L., & Ritzwoller, M. H. (2005). High-resolution surface-wave tomography from ambient seismic noise. *Science*, *307*(5715), 1615–1618.

Smith, M. L., & Dahlen, F. (1973). The azimuthal dependence of love and rayleigh wave propagation in a slightly anisotropic medium. *Journal of Geophysical Research*, *78*(17), 3321–3333.

Sollberger, D., Greenhalgh, S. A., Schmelzbach, C., Van Renterghem, C., & Robertsson,

J. O. (2018). 6-c polarization analysis using point measurements of translational and rotational ground-motion: theory and applications. *Geophysical Journal International*, *213*(1), 77–97.

Spudich, P., & Fletcher, J. B. (2008). Observation and prediction of dynamic ground strains, tilts, and torsions caused by the m w 6.0 2004 parkfield, california, earthquake and aftershocks, derived from upsar array observations. *Bulletin of the Seismological Society of America*, *98*(4), 1898–1914.

Spudich, P., Steck, L. K., Hellweg, M., Fletcher, J., & Baker, L. M. (1995). Transient stresses at parkfield, california, produced by the m 7.4 landers earthquake of june 28, 1992: Observations from the upsar dense seismograph array. *Journal of Geophysical Research: Solid Earth*, *100*(B1), 675–690.

Stehly, L., Campillo, M., & Shapiro, N. (2006). A study of the seismic noise from its long-range correlation properties. *Journal of Geophysical Research: Solid Earth*, *111*(B10).

Tang, L., & Fang, X. (2021a). Generation of 6-c synthetic seismograms in stratified vertically transversely isotropic media using a generalized reflection and transmission coefficient method. *Geophysical Journal International*, *225*(3), 1554–1585.

Tang, L., & Fang, X. (2021b). Numerical study of the application of six-component ambient seismic noise data for high-resolution imaging of lateral heterogeneities. In *Seg/aapg/sepm first international meeting for applied geoscience & energy.*

Tang, L., & Fang, X. (2023). Application of six-component ambient seismic noise data for high-resolution imaging of lateral heterogeneities. *Geophysical Journal International*, *232*(3), 1756–1784.

Tang, L., Igel, H., & Montagner, J.-P. (2023a). Anisotropy and deformation processes in southern california from rotational observations. *Geophysical Research Letters*, *50*(23), e2023GL105970. Retrieved from `[Dataset].https://doi.org/10.1029/2023GL105970.`

Tang, L., Igel, H., & Montagner, J.-P. (2023b). Single-point dispersion measurement of surface waves combining translation, rotation and strain in weakly anisotropic media: theory. *Geophysical Journal International*, *235*(1), 24–47.

Tanimoto, T., & Prindle, K. (2007). Surface wave analysis with beamforming. *Earth, planets and space*, *59*, 453–458. Retrieved from `[Dataset].https://doi.org/10.1186/BF03352706.`

Tape, C., Liu, Q., Maggi, A., & Tromp, J. (2009). Adjoint tomography of the southern california crust. *Science*, *325*(5943), 988–992.

Wassermann, J., Wietek, A., Hadziioannou, C., & Igel, H. (2016). Toward a single-station approach for microzonation: Using vertical rotation rate to estimate love-wave dispersion curves and direction finding. *Bulletin of the Seismological Society of America*, *106*(3), 1316–1330.

Wu, S., Jiang, C., Schulte-Pelkum, V., & Tong, P. (2022). Complex patterns of past and ongoing crustal deformations in southern california revealed by seismic azimuthal anisotropy. *Geophysical Research Letters*, *49*(15), e2022GL100233. Retrieved from `[Dataset].https://doi.org/10.1029/2022GL100233.`

Yang, Z., Sheehan, A., & Shearer, P. (2011). Stress-induced upper crustal anisotropy in southern california. *Journal of Geophysical Research: Solid Earth*, *116*(B2). Retrieved from `[Dataset].https://doi.org/10.1029/2010JB007655.`

Yuan, S., Gessele, K., Gabriel, A.-A., May, D. A., Wassermann, J., & Igel, H. (2021). Seismic source tracking with six degree-of-freedom ground motion observations. *Journal of Geophysical Research: Solid Earth*, *126*(3), e2020JB021112.

Zembaty, Z., Bernauer, F., Igel, H., & Schreiber, K. U. (2021). *Rotation rate sensors and their applications* (Vol. 21) (No. 16). MDPI.

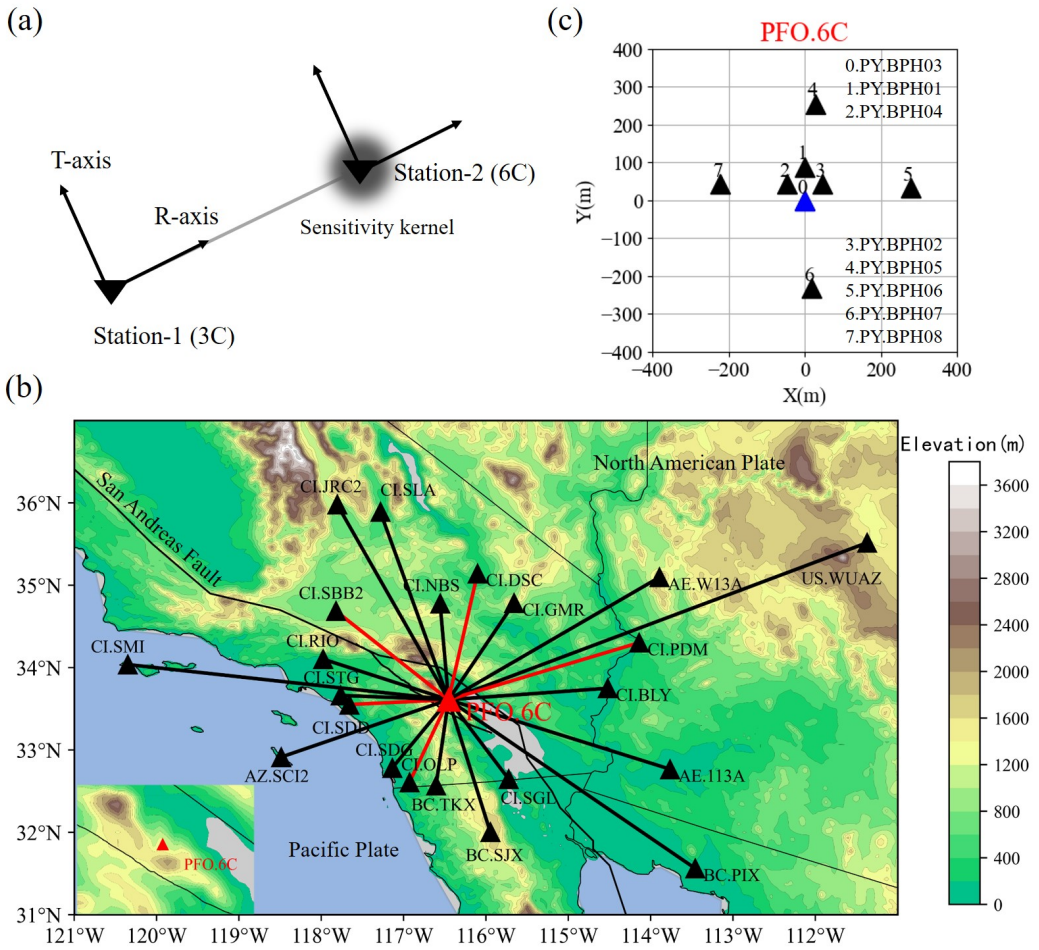

Figure 1. (a) Schematic diagram of a sensitivity kernel of the amplitude ratio method in Equations (1-3) from 6C CCFs of a pair of stations. Station-1 has three-component (3C) translational displacement. Station-2 has three-component translational displacement and three-component rotation (6C). (b) Distributions of broadband seismic stations. The black triangles represent 3C stations. The red triangle represents the 6C station of Piñon Flat Observatory (PFO) while the rotational waveform is retrieved from the ADR approach using a small seismic array of (c). (c) Reference PFO.6C array which is used to retrieve rotational motions from ambient noise data. At the blue station the translational and rotational components are compared.

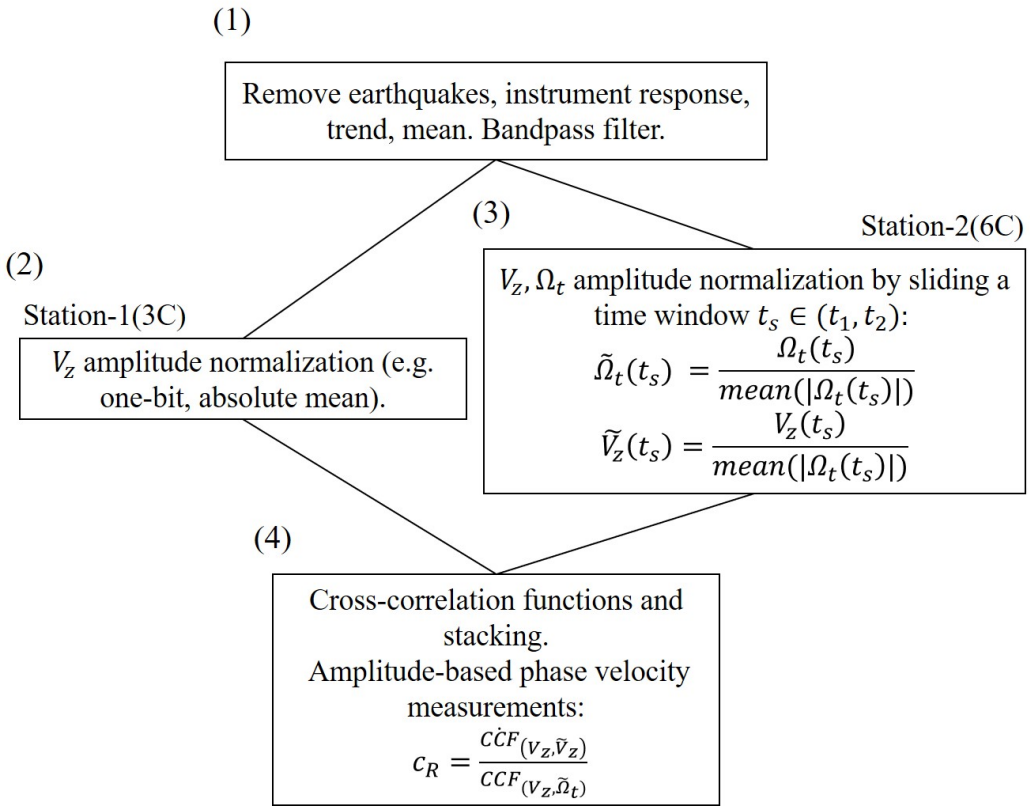

Figure 2. Schematic representation of the 6C ambient noise data processing scheme. (1): single-station preprocessing. (2): 3C station time domain normalization. (3): 6C station time domain normalization. (4): Calculate CCFs and phase velocity estimation.

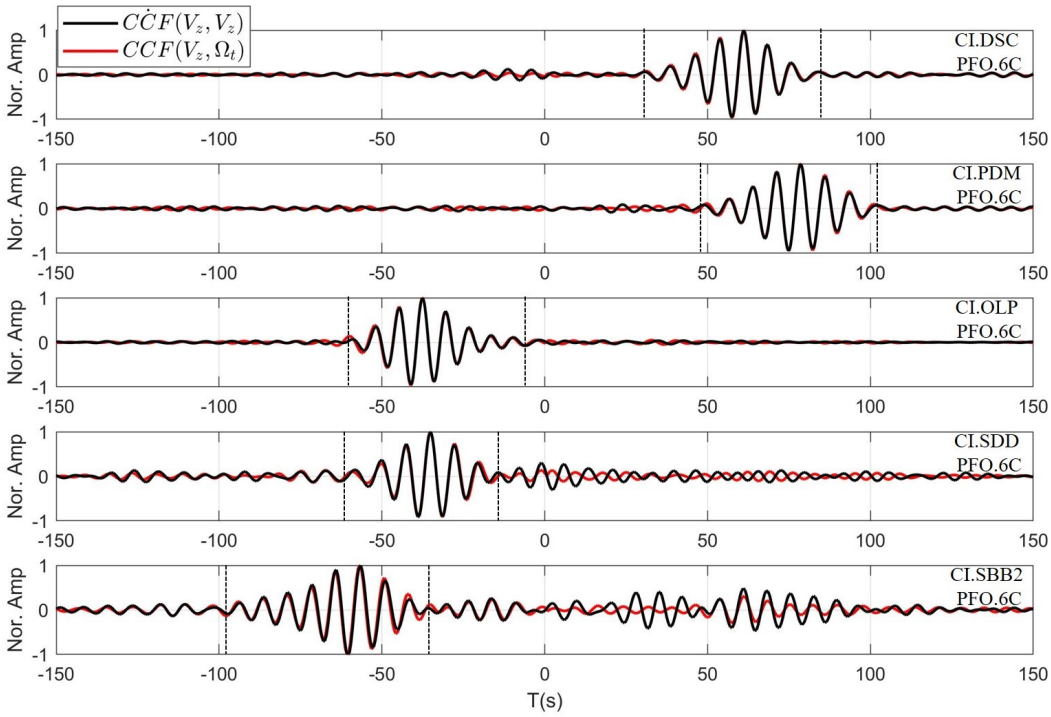

Figure 3. Rayleigh wave waveform (marked by black dashed lines) comparison (7s-12s) of CCFs calculated using one-year ambient noise data from five pairs of stations (CI.DSC, CI.PDM, CI.OLP, CI.SDD, CI.SBB2 and PFO.6C). The red lines represent CCFs between vertical translation of 3C station and transverse rotation of 6C station. The black lines represent CCFs between vertical translation of 3C station and vertical translation of 6C station. Red lines in Figure 1b represent their great circle paths.

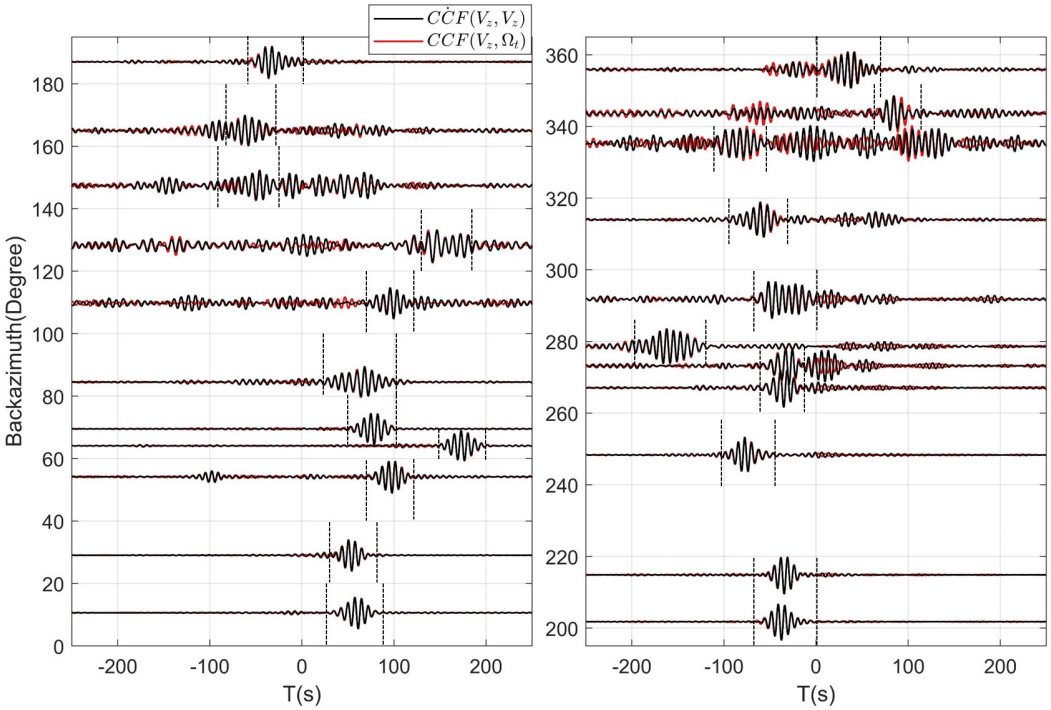

Figure 4. Normalized CCFs (marked by black dashed lines) of 7-12s in the azimuth domain based on Equation (1). The red lines represent CCFs between vertical translation of 3C station and transverse rotation of 6C station. The black lines represent CCFs between vertical translation of 3C station and vertical translation of 6C station.

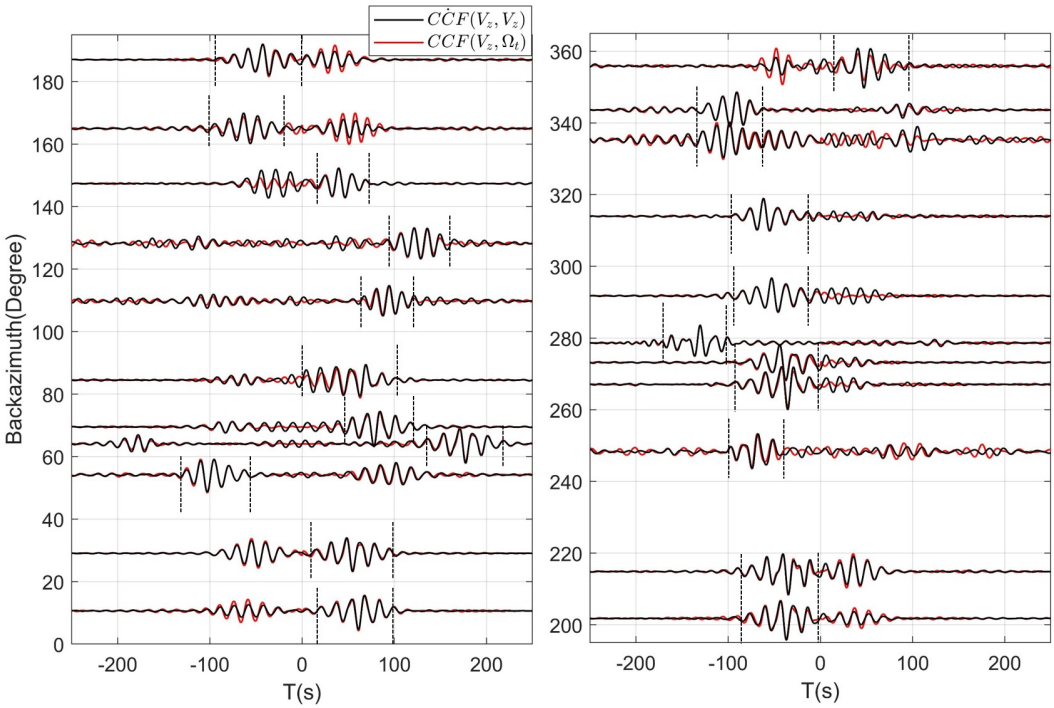

Figure 5. Normalized CCFs (marked by black dashed lines) of 12-20s in the azimuth domain based on Equation (1). The red lines represent CCFs between vertical translation of 3C station and transverse rotation of 6C station. The black lines represent CCFs between vertical translation of 3C station and vertical translation of 6C station.

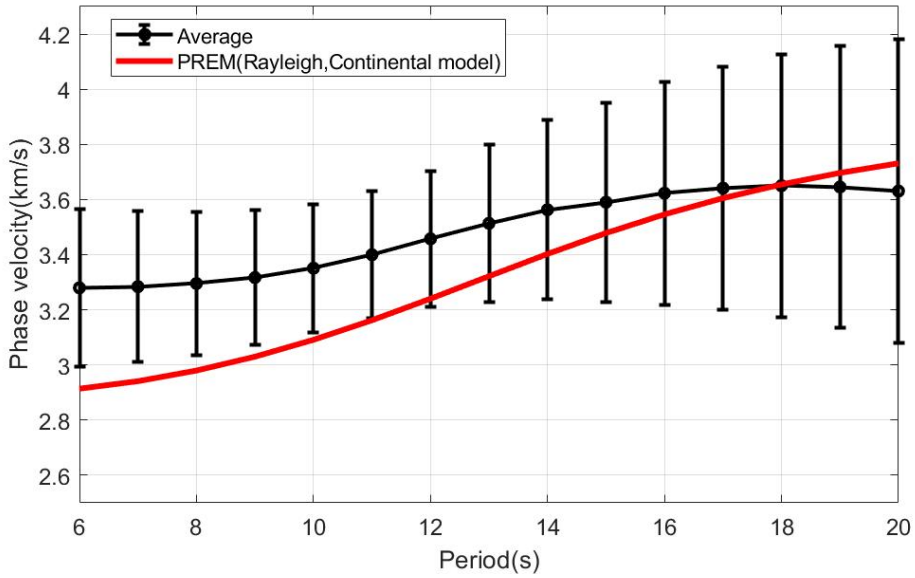

Figure 6. Average phase velocity of Rayleigh waves at 6-20s from 22 pairs of CCFs in Figure 4 and Figure 5.

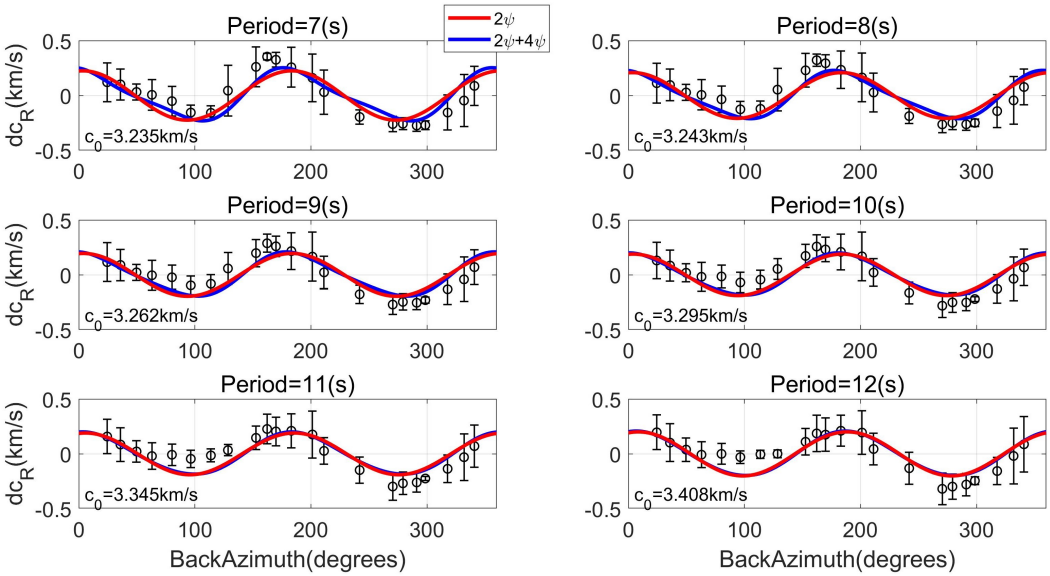

Figure 7. Velocity variation of 7-12s of Rayleigh waves in the azimuth domain. Red lines are the best-fit 2ψ curves and blue lines are the best-fit curves when 2ψ and 4ψ terms are included in Equation (4).

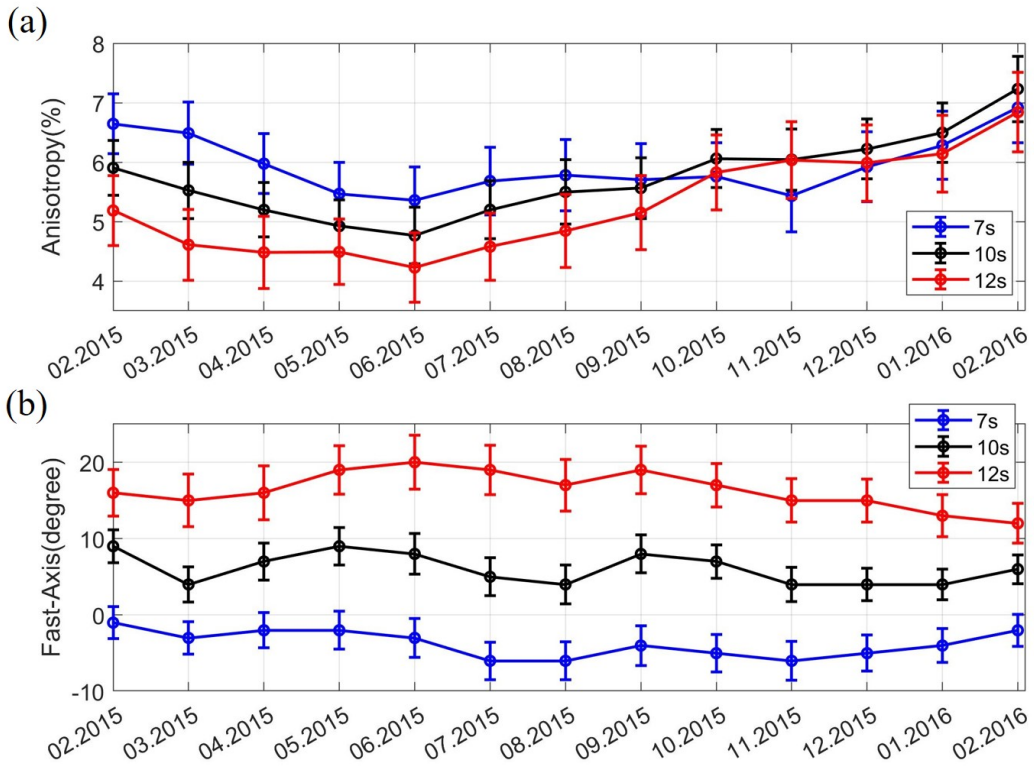

Figure 8. Seasonal variation of anisotropy and fast axis with sliding window of two months. (a) Seasonal variation of peak-to-peak anisotropy of the 2ψ+4ψ term at 7s(blue lines), 10s (black lines) and 12s (red lines). (b) Seasonal variation of fast-axis of the 2ψ+4ψ term at 7s(blue lines), 10s (black lines) and 12s (red lines).

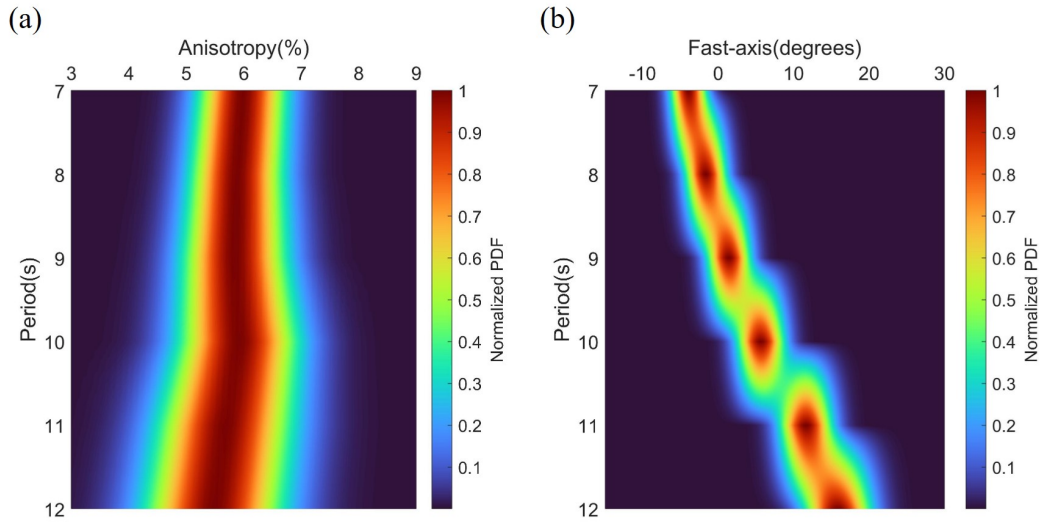

Figure 9. Normalized probability density function of peak-to-peak anisotropy and fast-axis after averaging one-year data. (a) Peak-to-peak anisotropy after averaging the result of Figure 8a. (b) Fast-axis after averaging the result of Figure 8b.

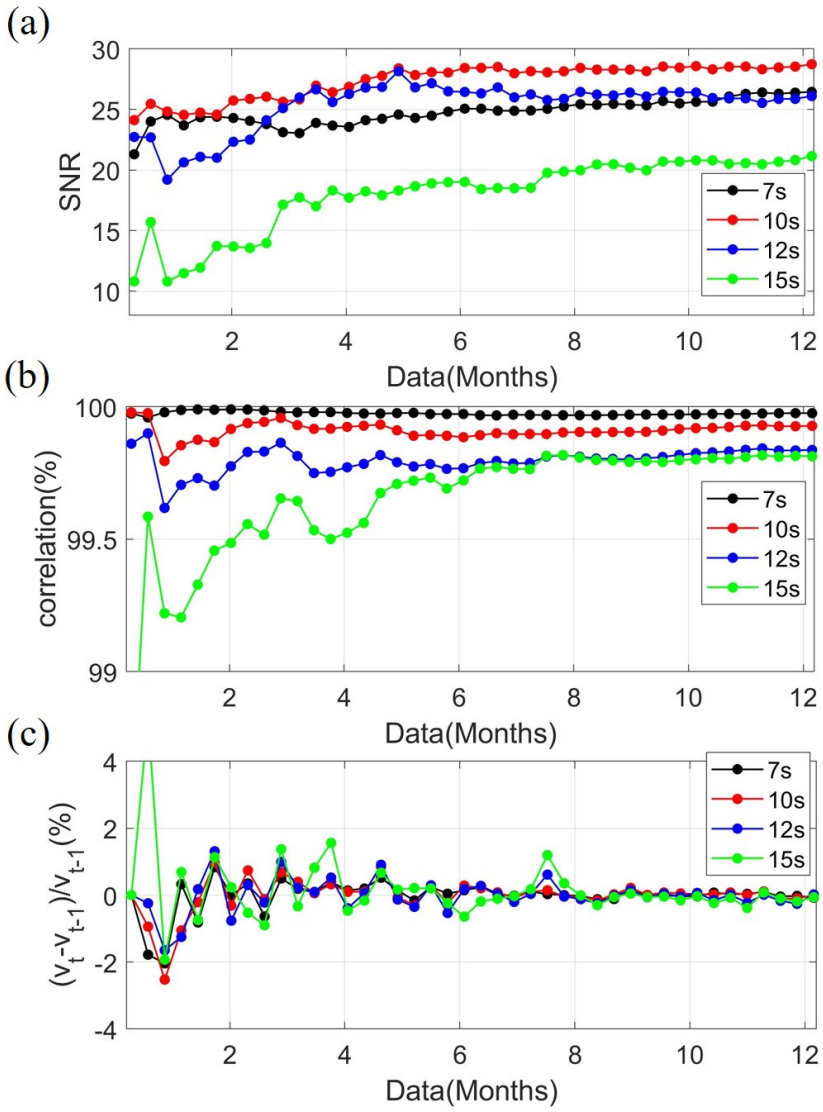

Figure 10. Stability of CCFs between CI.PDM station and PFO.6C station. (a) Signal-to-noise ratio (SNR) of $C\dot{C}F_{(V_{z1},V_{z2})}$ at four periods (7s, 10s, 12s, and 15s) using different data volume. (b) Correlation coefficients between $C\dot{C}F_{(V_{z1},V_{z2})}$ and $CCF_{(V_{z1},\Omega_{t2})}$ at four periods (7s, 10s, 12s, and 15s) using different data volume. (c) Relative velocity variation $(c_T - c_{T-1})/c_{T-1}$ at four periods (7s, 10s, 12s, and 15s) using different data volume.

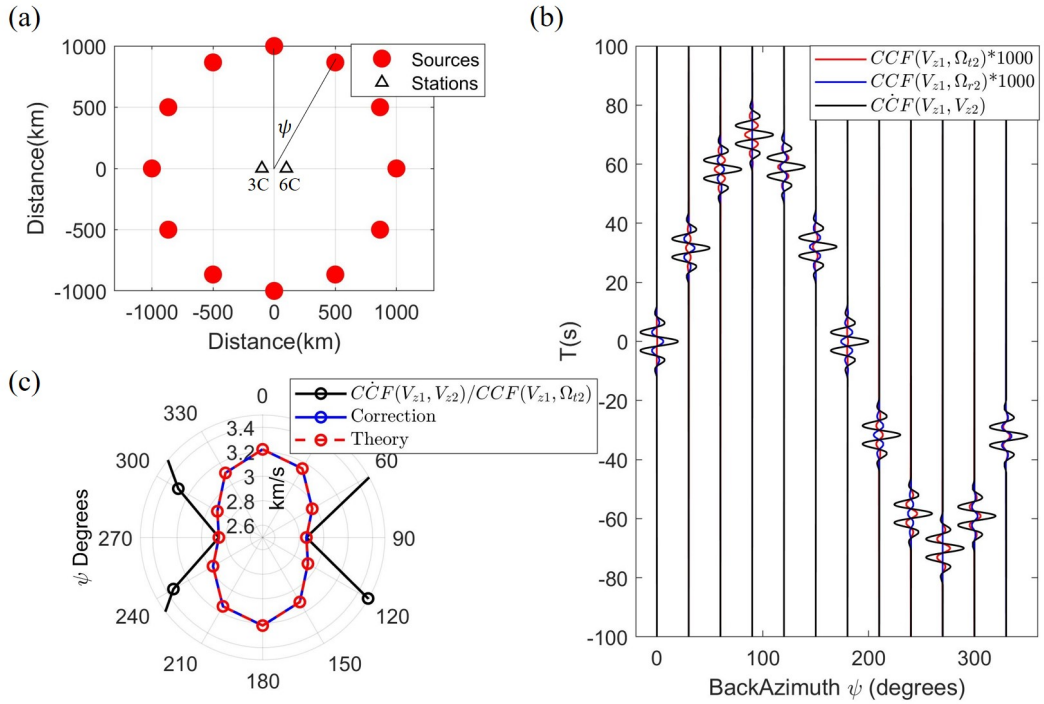

Figure 11. (a) Distributions of seismic sources (vertical force source) and a pair of stations for investigating the effect of noise source in the non-stationary zone of Figure S3c. The analytical phase velocity of Rayleigh waves is $V_R = 3.258 + 0.194 * cos(2\psi) + 0.025 * sin(2\psi)$. (b) Synthetic CCFs from the model of (a) after normalizing the amplitude of $C\dot{C}F_{(V_{z1},V_{z2})}$. (c) Velocity estimation using CCFs of (b). The black line represents the results from Equation (1) which show large error compared with the analytical solution marked by red points. The blue line represents the corrected results of replacing $CCF_{(V_{z1},\Omega_{t2})}$ with $\sqrt{CCF^2_{(V_z1,\Omega_t2))} + CCF^2_{(V_z1,\Omega_r2))}}$.

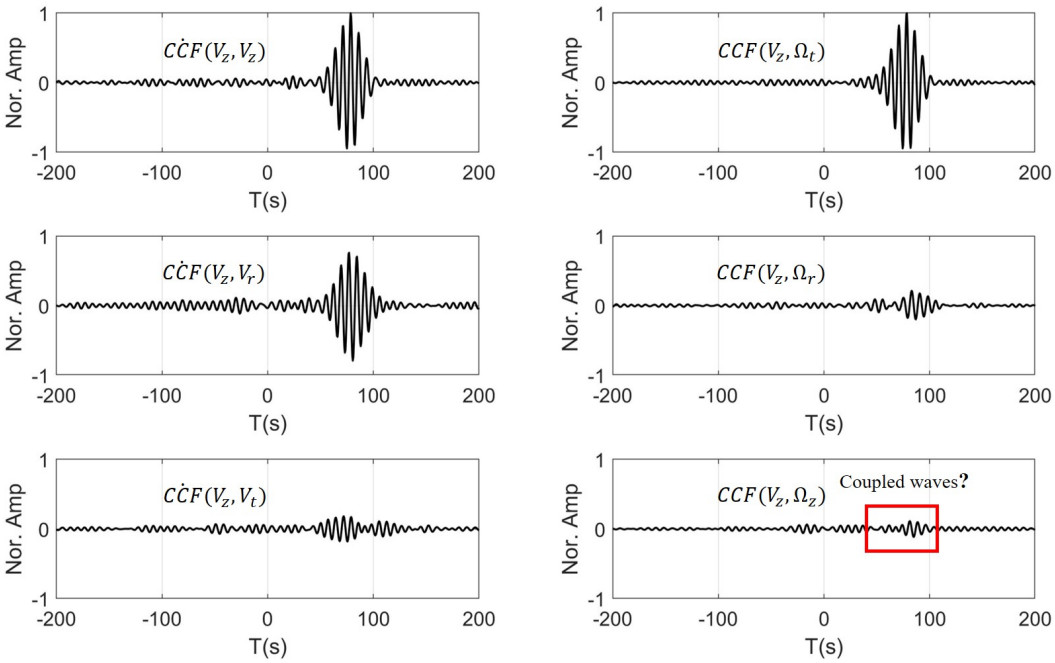

Figure 12. CCFs (7-12s) between vertical translation of the CI.PDM station and PFO.6C station using one-year ambient noise data.

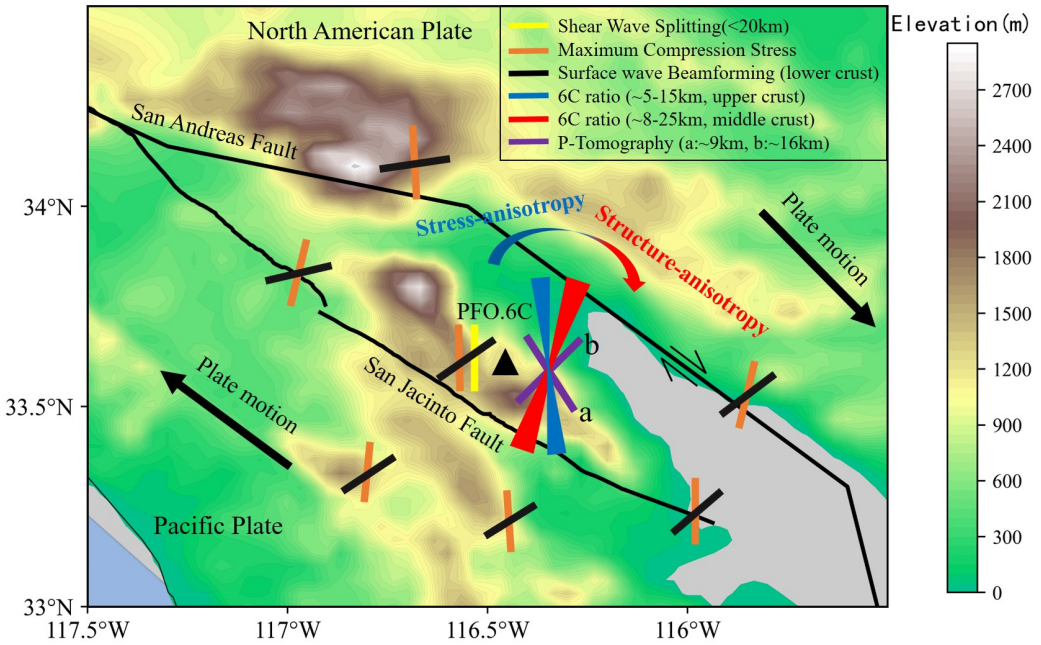

Figure 13. Stress and structure-induced anisotropy revealed from 6C observations. The blue line shows the fast-axis of Rayleigh waves in the upper crust associated with the stress-induced anisotropy. The red line shows the fast-axis of Rayleigh waves in the middle crust associated with the structure-induced anisotropy. Curved arrows represent transitions of anisotropy mechanisms (from stress-induced anisotropy to structure-induced anisotropy). The orange lines represent the maximum compression stress directions near PFO array, which are determined from borehole breakouts, hydraulic fracturing experiments, and earthquake focal mechaism inversions (Heidbach et al., 2010). The yellow line represents the fast-axis direction of shear-wave splitting at PFO using local events, which is sensitive to upper crustal structure (<20km) (Yang et al., 2011). The black lines represent the fast-axis directions of surface waves using the beamforming tomography method (Tanimoto & Prindle, 2007). The purple line-a and line-b represent the fast-axis directions of P waves at around 9km and 16km, respectively, using the P wave tomography method (Wu et al., 2022). The black arrows show the plate motion directions (Tang et al., 2023a).